



This is a repository copy of *Bridging the gap between microstructurally resolved computed tomography-based and homogenised Doyle-Fuller-Newman models for lithium-ion batteries*.

White Rose Research Online URL for this paper:

<https://eprints.whiterose.ac.uk/224261/>

Version: Published Version

Article:

Tredenick, E.C. orcid.org/0000-0001-9105-2858, Boyce, A.M. orcid.org/0000-0002-8164-1808, Wheeler, S. orcid.org/0000-0002-4503-4621 et al. (6 more authors) (2025) Bridging the gap between microstructurally resolved computed tomography-based and homogenised Doyle-Fuller-Newman models for lithium-ion batteries. *Journal of The Electrochemical Society*, 172 (3). 030503. ISSN 0013-4651

<https://doi.org/10.1149/1945-7111/adb684>

Reuse

This article is distributed under the terms of the Creative Commons Attribution (CC BY) licence. This licence allows you to distribute, remix, tweak, and build upon the work, even commercially, as long as you credit the authors for the original work. More information and the full terms of the licence here:

<https://creativecommons.org/licenses/>

Takedown

If you consider content in White Rose Research Online to be in breach of UK law, please notify us by emailing eprints@whiterose.ac.uk including the URL of the record and the reason for the withdrawal request.



eprints@whiterose.ac.uk
<https://eprints.whiterose.ac.uk/>

OPEN ACCESS

Bridging the Gap between Microstructurally Resolved Computed Tomography-Based and Homogenised Doyle-Fuller-Newman Models for Lithium-Ion Batteries

To cite this article: E. C. Tredenick *et al* 2025 *J. Electrochem. Soc.* **172** 030503

View the [article online](#) for updates and enhancements.

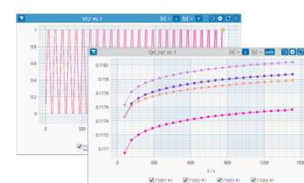
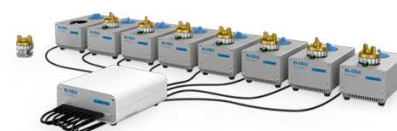
You may also like

- [Roadmap on Li-ion battery manufacturing research](#)
Patrick S Grant, David Greenwood, Kunal Pardikar et al.
- [Targeted hydrolysis and deprecipitation of \$Mn_2AlC\$ precipitates: a route to a novel precursor of rare earth free MnAl-C permanent magnets](#)
Florian Jürries, Lukas Beyer, Kornelius Nielsch et al.
- [A continuum of physics-based lithium-ion battery models reviewed](#)
F Brosa Planella, W Ai, A M Boyce et al.

PAT-Tester-x-8 Potentiostat: Modular Solution for Electrochemical Testing!

EL-CELL[®]
electrochemical test equipment

- ✓ **Flexible Setup with up to 8 Independent Test Channels!**
Each with a fully equipped Potentiostat, Galvanostat and EIS!
- ✓ **Perfect Choice for Small-Scale and Special Purpose Testing!**
Suited for all 3-electrode, optical, dilatometry or force test cells from EL-CELL.
- ✓ **Complete Solution with Extensive Software!**
Plan, conduct and analyze experiments with EL-Software.
- ✓ **Small Footprint, Easy to Setup and Operate!**
Usable inside a glove box. Full multi-user, multi-device control via LAN.



Contact us:

☎ +49 40 79012-734

✉ sales@el-cell.com

🌐 www.el-cell.com



Bridging the Gap between Microstructurally Resolved Computed Tomography-Based and Homogenised Doyle-Fuller-Newman Models for Lithium-Ion Batteries

E. C. Tredenick,^{1,2,z} A. M. Boyce,^{2,3,4} S. Wheeler,^{2,5} J. Li,^{2,3} Y. Sun,^{2,5} R. Drummond,⁶ S. R. Duncan,^{1,2} P. S. Grant,^{2,5} and P. R. Shearing^{1,2,3}

¹Department of Engineering Science, University of Oxford, Oxford, OX1 3PJ, United Kingdom

²The Faraday Institution, Quad One, Harwell Campus, Didcot, OX11 0RA, United Kingdom

³Electrochemical Innovation Lab, Department of Chemical Engineering, University College London, London, WC1E 7JE, United Kingdom

⁴School of Mechanical and Materials Engineering, University College Dublin, Dublin, Ireland

⁵Department of Materials, University of Oxford, Oxford, OX1 3PH, United Kingdom

⁶Department of Automatic Control and Systems Engineering, University of Sheffield, Sheffield, S1 3JD, United Kingdom

Lithium-ion batteries (LIB) are synonymous with the modern age of electrification, yet advances in battery design, manufacturing, and chemistry are still urgently needed. Mathematical modelling plays an important role in understanding LIB performance and can provide physics informed design directions, optimisation and explain outcomes. We present an exploration and detailed comparison of the commonly used homogenised Doyle-Fuller Newman (DFN) model and X-ray computed tomography (CT) based microstructural model for LIBs, along with experimental data. We provide insights into the relative benefits of each model and highlight why they are important to battery technology development. We compare two common cathode chemistries, lithium nickel manganese cobalt oxide (NMC), and lithium iron phosphate (LFP), and investigate discharge current density. The DFN and CT-based models show good agreement for averaged LIB metrics, such as the voltage response and active material utilization, demonstrating that homogenised, computationally inexpensive models are an essential basis for battery design and optimisation. The CT-based microstructural model provides further insight into localised particle and electrode dynamics, considering heterogeneities that are a source of battery degradation. Qualitatively, the models also compare well with experimental secondary ion mass spectrometry mapping of the Li concentration in the active particles across the electrode thickness.

© 2025 The Author(s). Published on behalf of The Electrochemical Society by IOP Publishing Limited. This is an open access article distributed under the terms of the Creative Commons Attribution 4.0 License (CC BY, <https://creativecommons.org/licenses/by/4.0/>), which permits unrestricted reuse of the work in any medium, provided the original work is properly cited. [DOI: 10.1149/1945-7111/adb684]



Manuscript submitted October 29, 2024; revised manuscript received January 21, 2025. Published March 5, 2025.

Supplementary material for this article is available [online](#)

As battery manufacturing continues to grow in response to the electrification of transport, the lithium-ion battery (LIB) is increasingly becoming a commoditised item. The LIB supply chain is predicted to grow by 30% annually, from a current level of 0.7 TWh per year to reach a market size of 4.7 TWh per year by 2030.¹ There is commercial advantage and growing pressure to accelerate the cell design and optimisation process and to reduce costs. Optimising cell design quickly is challenging for cell manufacturers because new battery materials and applications emerge frequently and often unexpectedly. Delivering design optimisation to meet these challenges can only be achieved by a shift away from a dependence on trial and error and move toward greater automation including the use of mathematical modelling.²

Many battery models have been developed to meet the needs of cell designers.^{3,4} The scope of these models is multiscale, going from the pack-level⁵ all the way down to simulating individual particles⁶ and molecules.⁷ The simplest class of battery models are those described by equivalent circuit models, which represent the current/voltage dynamics of the battery in terms of circuit elements such as resistors and capacitors.^{8–10} Due to the simplicity of these models and their computational efficiency, circuit models currently dominate applications where the value of an accurate current/voltage prediction is paramount, such as battery management systems (BMS) and pack-level modelling.¹¹ However, because equivalent circuit models abstract the underlying physics of the battery, they are generally not appropriate for cell design problems.

The most simple class of physics-based models are single particle models (SPM)¹² together with many variants that include those with electrolyte dynamics (SPMe),^{13–15} thermal effects,^{16,17} degradation,¹⁸ and the equivalent hydraulic model.¹⁹ The SPM/

SPMe models assume that the active particle Li concentration is uniform through the electrode thickness, an assumption that is not appropriate for the thick electrodes common in commercial cells and during fast charging cases considered here.

The benchmark model for LIB modelling is the Doyle-Fuller-Newman (DFN) framework, which is a physics-based continuum model incorporates porous electrode theory.^{14,20,21} The DFN model comprises a set of coupled partial differential Eqs. (PDEs), including nonlinear parabolic and elliptic PDEs. The DFN model is commonly 1D through the electrode thickness, and pseudo 1D through the radius of the spherical particle and is hence referred to as pseudo-two-dimensional (P2D), “pseudo-2D” (1 + 1D). A continuum based approach is used to describe the electrode microstructure, which includes a description of the carbon binder domain (CBD) and the interconnected pores, and the particles are assumed to be spherical and evenly distributed through the electrode thickness. Potentials in the solid particles and liquid electrolyte are modelled, along with the Li ion concentration in the particles and liquid electrolyte, and the reaction current density. The Python implementation PyBaMM²² uses the DFN model, building on DUALFOIL²³ code. Extensions of the DFN model have been considered recently and include multiple layers of different chemistries within the anode, cathode or both (M-DFN),²⁴ and the many particle DFN model (MP-DFN), which is able to consider an active particle size distribution.^{25,26} There are homogenised 3D DFN models (3 + 3D, which use three-dimensions to describe both the electrode and the particles), which can allow for more realistic descriptions, such as active particles that are not spherical, and particle cracking.^{3,21} A 3D model was compared to a 1D DFN model for NMC and the 1D was found to be generally suitable for the cases studied.²⁷ 3D microscopic, 3D homogenised and DFN-type models including active particle size distributions were compared for a 3C discharge of a LiCoO₂ (LCO) electrode,²⁶ providing important information including detailed voltage profiles.

^zE-mail: eloise.tredenick@eng.ox.ac.uk

There are different modelling approaches for lithium iron phosphate, LiFePO₄ (LFP) including single particles that are not described by spherical diffusion, but instead by phase behavior,^{6,28} and phase transitions using a shrinking core.²⁹

X-ray computed tomography (CT) imaging has only recently been applied to battery research and in general, CT is a relatively new tool for the electrochemical field⁴. CT image-based models are derived from the experimental reconstructed 3D CT scan images that resolve active materials, binder and pores. The image is filtered, segmented and then a computational mesh is constructed to facilitate the application of the model including electrochemical and transport-based partial differential Eqs. on a geometry that is representative of the real microstructure. CT image-based models are continuum models and allow spatial resolution of the collection of particles within a volume that can be statistically representative of the electrode volume if large enough. Image-based models are able to capture the realistic shape of particles, accounting for the non-spherical geometry and non-uniform dispersion within the electrode volume, and both of these factors have been shown to play a key role in battery performance and long term degradation.³⁰ In some cases, given sufficient CT imaging resolution and computational resources, it is possible to resolve the microstructural details within the CBD. However, this detail is often homogenised due to the lack of CT imaging resolution or to maintain practical computation times. CT image-based models use similar Eqs. to the P2D DFN model, but the particle size is implicit within the model, and the CBD, if resolved, is modelled as a separate electrically conductive medium. CT image-based models are resolved in 3D across the electrode thickness, including the particle in 3D. The model is created by discretising the segmented CT image to mesh elements. Since the governing electrochemical and transport Eqs. are solved for the exact geometry, it is possible to probe the influence of local heterogeneities, such as variations in pore and particle size, shape and distribution.^{4,30–32} The electrochemical descriptions can be coupled with Li intercalation or de-intercalation induced stresses in the active particles, and for example the influence of particle voids on degradation behavior can be investigated.³³

The relative advantages and disadvantages of the DFN and microstructural CT model are summarised in Table I. While the CT model simulations are information-rich, the drawbacks of

solving the model with high spatial resolution are the computational demand and complexity,⁴ along with the need for high resolution CT scanners. Careful consideration about field of view (FOV) and resolution is required to represent the domain accurately. For problems such as estimating the model parameters, this computational effort can be limiting.

There have been limited comparisons of image based to DFN models, although one study has been carried out, showing a brief comparison of voltage data for LFP electrodes with good agreement but did not consider the full details of the CBD.³⁴ A detailed comparison of the two modelling approaches has been presented,³⁵ which showed close agreement between the two approaches, but this study only considered low C rates and did not include experimental data. Two further studies have compared the two models briefly for voltage profiles.^{36,37} One study³⁸ produced close agreement with a CT and 3D+1D DFN model including ellipsoid geometries, but only compared one chemistry, one C rate and did not include experimental data.

LIB experiments commonly focus on the electrode voltage response, whereas physics-based models can reveal electrode internal processes, such as the underlying Li ion concentration profiles and spatially-resolved potential responses. Further, much of a LIB's practical performance relates to Li dynamics within the electrode. Unfortunately, spatially and chemically resolving the local Li concentrations in the active particles by experiments, such as various types of electron or other microscopies, is difficult. A promising experimental technique is plasma focused ion beam/secondary ion mass spectrometry (PFIB/SIMS), which allows qualitative visualisation of the active particle concentration gradients at the scale of the electrode thickness, at a particular point in the charge or discharge.^{4,39–43} A comparison of CT and PFIB/SIMS imaging techniques is shown in Table II.

In this paper, we compare the homogenised modelling approach of the DFN model with the CT image-based microstructural model. These two models contain the same physics, with similar governing equations, but are resolved over different domains. We aim to understand the effects of non-uniform particle and electrolyte gradients through the electrode thickness, when discharging at high C rates (1C, 2C, 5C) and for relatively thick (80 μm, 90 μm and 160 μm) electrodes. We apply the models to two electrode

Table I. Comparison of DFN and CT scan domain models, where ϵ is the electrolyte volume fraction, b is the tortuosity and R is the particle radius. A “+” indicates a favourable option, “*” an intermediate option and “×” an unfavourable option.

	DFN model - averaged domain	CT scan domain
Experimental data validation accuracy	✓ ⁺	✓ ⁺
Computation Time	Seconds ⁺	Hours to days [×]
Geometry	Additional parameters required for ϵ , b or R [×]	Particles are explicitly resolved. Macropores and bulk carbon binder may be resolved depending on CT resolution. The micropores within the carbon binder domain are difficult to resolve and are accounted for via a Bruggeman homogenisation method or tortuosity relationships. [*]
Special domain features	Capture porosity and particle size distributions through the electrode, change the electrode thickness and volume fraction. ⁺	Ability to modify volume fraction and electrode volumes can be cloned, mirrored and stacked to extend the electrode thickness. ³⁰⁺
Dimensions	1D in x (through electrode), plus 1D (pseudo) in r (spherical particle radius), so pseudo-2D (1+1D) [*]	3D in x , y , z . ⁺
Limitations	New equations required for non-spherical particles [*]	Resolution of desired geometrical features is dependent on limitations of CT instrument and morphology of the microstructure in question, such as inability to capture LFP CBD. Limited FOV that can cause representation issue. Inability to capture CBD microporosity. [*]
Software required	MATLAB [®] , Python, C ⁺⁺ , PyBaMM and others	A combination of Simpleware ScanIP meshing and COMSOL [®] MultiPhysics finite element commercial software, or Python and C ⁺⁺ based open source software such as FEniCS or OpenFOAM and others.
Optimisation	✓ ⁺	✓Possible but involves increased computation times. [*]

Table II. CT compared to PFIB/SIMS imaging techniques⁴ including common minimum resolutions and field of view (FOV), along with those used in this study shown with an “*” and the minimum resolution values may take additional effort and a minimum of 100 nm resolution for PFIB/SIMS is common.

Technique	Resolution	Resolution*	FOV	FOV*	Sample Preservation	Vacuum Requirement	Information Extracted
X-ray CT (nano-)	~ 10 nm	64 nm (50 nm possible)	~ 100 μm	64 μm \times 64 μm (16 μm \times 16 μm possible)	Non-destructive	n/a	Porosity, surface area, tortuosity, chemical composition
PFIB/SIMS	~ 10 nm	360 nm (100 nm possible)	~ 10 μm	50 μm \times 105 μm (min depends on spot size and scan resolution)	Destructive	Vacuum required	Porosity, light and trace element mappings

Table III. Timings of DFN model code in MATLAB[®] 2023a, and CT scan model in COMSOL[®] MultiPhysics, for NMC (80 μm) and LFP (90 μm), both at a 1C discharge. N is the number of nodes in each particle radius, r and through thickness compartment, x , and $N = 11$ is for testing purposes only. The “*” indicates the fine mesh for plotting the article figures. The DFN model was solved on a Dell, Windows 10 desktop PC, Intel^(R) Core, i7-10700 CPU @ 2.9GHz, 16 GB (average practical usage 2.5 GB), random access memory (RAM), 64 bit system. The CT model was solved on a Dell, Windows 10 workstation PC, Intel^(R) Xeon^(R), Platinum 8260 CPU @ 2.4GHz, 64 bit, 750 GB RAM (average practical usage 100 GB), high-performance computer.

	N	States	Run time
NMC - DFN	11, 11	154	0.7 s
	27, 27	810	4.4 s
	35, 55*	2,130	20.4 s
NMC - CT	7.3×10^6	8.3×10^6	8 hr
LFP - DFN	11, 11	154	0.35 s
	27, 27	810	4.2 s
	43, 65*	3,034	49.9 s
LFP - CT	4.3×10^6	6.9×10^6	15 hr

chemistries of lithium nickel manganese cobalt oxide, Li[Ni_{0.6}Co_{0.2}Mn_{0.2}]O₂ (NMC622), and lithium iron phosphate, LiFePO₄ (LFP), to avoid chemistry-specific conclusions. The model outputs are compared to standard voltage experiments and to PFIB/SIMS based Li mapping across an LFP electrode. The novelty of our approach is a thorough comparison of the two models over a range of operating conditions and chemistries, including active material and electrolyte concentration, voltage profiles and SOC in parallel to electrochemistry experiments that are validated with the models, along with independent PFIB/SIMS Li mapping.

Methods

Mathematical models and parameters.—*Numerical solution procedure.*—The finite volume DFN model, which is described in Supplementary Eqs. (S1) to (S7), is nondimensionalised and solved numerically, by discretising the model’s PDEs using second order central differences to approximate the spatial derivatives, along with averaging of the diffusivity and conductivity functions at the control volume faces. The resulting system of differential algebraic Eqs. (DAEs) is solved using “ode15s” including a mass matrix, within MATLAB[®] 2023a.⁴⁴ Timings for the code solutions for a 1C discharge are shown in Table III. Parameters are shown in Table IV and the fitting is based on the four cases for NMC-based electrodes and the LFP-based electrode at 5C, using the same parameters between the DFN and CT models where possible, with the fit being focused on the voltage experimental data. The parameters are fitted to minimize the difference between the model

and experiment. The DFN simulation and post-processing codes that have been used to produce the results of this study are available as open-source code (https://github.com/EloiseTrednick/DFN-P2D-Matlab-NMC622-LFP_CTvsDFN).

The CT image-based model is solved using the finite element method. Simpleware ScanIP (Mountain View, CA, USA) is used to discretise the segmented image, giving linear tetrahedral meshes with the quantity of mesh elements and degrees of freedom shown in Table III. A mesh sensitivity test was carried out and the simulation conditions were found to be stable. The electrochemical and transport Eqs. as outlined in Supplementary Eqs. (S13) to (S16), are solved in COMSOL[®] MultiPhysics (v6.1, Sweden). Time stepping is handled using 2nd order backward Euler differentiation. The volume fraction of the CBD and electrolyte are explicitly resolved within the CT model for the NMC electrode. For the LFP electrode, the much finer scale CBD microstructure could not be captured via X-ray CT due to resolution limitations and was therefore instead modelled using a homogenised approach, similar to the P2D DFN model, where an averaged value of the volume fraction of CBD and electrolyte is used throughout the domain (Supplementary Eqs. (S15a) to (S15c)).

The parameter values (Table IV) for the reaction rates, k_p are fitted and align with those found elsewhere,^{45,50} along with the initial concentrations in the solid particles, $c_{s,0}$,⁵¹ and solid particle diffusivity for LFP, $D_{s,p}$.⁵² The parameters between the DFN and CT models in Table IV are either the same or similar in most cases, and for LFP the DFN model has the same parameters as the CT model except for $\varepsilon_{e,p}$. For the DFN parameter for LFP, the porosity, $\varepsilon_{e,p}$, is taken from experimental results as it is calendered to 30% porosity, and then fitted further to 0.2625. For NMC, the differences in the electronic conductivities in the solid, $\sigma_{s,p}$, between the CT and DFN models are to be expected due to the CBD being defined explicitly for the CT model only. For the DFN model, a resistance is added for NMC as it is known to have higher internal resistance than LFP.⁵³ A function for the solid particle diffusivity, D_s , was considered, but this did not alter the results significantly, so was not used further.

Experiment.—*LFP cell fabrication.*—Electrodes manufactured comprise LFP (MTI, USA), carbon additive (C65, Imerys, UK), and polyvinylidene fluoride binder (PVDF, Solef 5130, Solvay, UK). Active materials and carbon additive are dried overnight under vacuum and a 3wt.% PVDF in 1-Methyl-2-pyrrolidinone (NMP, Sigma) solution was then produced by stirring overnight. The electrode slurry is produced by mixing the 3wt.% PVDF in NMP solution with the active material and carbon conductive additive using a planetary mixer (Thinky ARE-250). The solid material mass fraction ratio is 92:4:4 (active material: carbon additive: binder) for the slurry, with a solid content fraction of 40%, targeting an electronic conductivity of 5 S/m. The electrode slurry is cast onto carbon-coated aluminum foil (MTI, 18 μm total thickness) using a doctor blade and drawdown table. Dried electrode sheets are calendered to a thickness that resulted in a porosity of 30%.

Table IV. Model parameters for NMC622 and LFP based electrodes. The “Exp” values are measured. If the CT model parameters that are derived from the X-ray CT image were different to the DFN model, they are shown in brackets as “(CT ...)”. If the Source denotes ‘CT image’, then the parameter was determined from the CT image scan data. *Average particle radius was determined from the CT scan data.

Parameter	Description	Unit	NMC	LFP	Source
A	Electrode cross-sectional area	m^2	9×10^{-10}	1×10^{-10}	CT image
b_p	Bruggeman tortuosity factor	—	1.5 (CT n/a)	2.3	Fitted, CT image
b_s		—	1.5	1.5	Fitted
c_{e0}	Initial concentration of Li ions in electrolyte	mol/m^3	1,000	1,000	Exp
$c_{s,p,0}$	Initial concentration of Li ions in solid particles	mol/m^3	12,662	570	Fitted
$c_{s,p,max}$	Maximum concentration of Li ions in solid particles	mol/m^3	48,700	22,806	45 46
$D_{s,p}$	Diffusivity of Li ions in solid	m^2/s	3.995×10^{-14}	1×10^{-15}	NMC 47, Fitted 48
F	Faraday constant	sA/mol	96485.332	96485.332	
g	Thermodynamic factor (equivalent to $(1 + \frac{\partial \ln f}{\partial \ln c_e})$)	—	1.43	1.43	
I	Current density	A/m^2	$I = I_c/A$		
I_c	Applied current	mA	$3.14 \times 10^{-5}, 1.57 \times 10^{-4}, 6.29 \times 10^{-5}, 3.14 \times 10^{-4}$ (1C, 5C 80 μm , 1C, 5C 160 μm)		$5.56 \times 10^{-6}, 1.38 \times 10^{-5}$ (2C, 5C)
k_p	Reaction rate constant	$m^{2.5}s^{-1}mol^{-0.5}$	7.5×10^{-12} (CT 9×10^{-12})	1.25×10^{-12}	Fitted
L_p	Thickness	μm	80, 160	90	CT image, Exp
L_s		μm	16	16	Exp 48
R	Universal gas constant	J/K/mol	8.314463	8.314463	
R_c	Internal resistance	Ωm^2	1.8×10^{-3} (CT n/a)	n/a	
R_p	Radius of particle	μm	4.9*	0.4*	CT image
T	Constant absolute reference temperature	K	293.15 (20 °C)	293.15 (20 °C)	Exp
t^+	Transference number of the electrolyte	—	0.37	0.37	49
$\varepsilon_{CBD,p}$	Carbon binder domain volume fraction	—	0.135 (CT n/a)	0.25	Fitted
$\varepsilon_{e,p}$	Electrolyte volume fraction	—	0.3 (CT n/a)	0.2625 (CT n/a)	Fitted
$\varepsilon_{e,s}$		—	1 (CT n/a)	1 (CT n/a)	Exp
$\sigma_{s,p}$	Electronic conductivity in solid	S/m	5 (CT 0.17)	5	Exp
σ_{CBD}	Electronic conductivity in CBD	S/m	n/a (CT 10)	—	Exp

Table V. Information for the NMC half cell.

Description	Value
Specific capacity at 0.05C	175 mAh/g
Min Voltage	2.5 V
Max Voltage	4.2 V

Table VI. Information for the LFP half cell.

Description	Value
Specific capacity at 0.05C	150 mAh/g
Min Voltage	2.5 V
Max Voltage	4.2 V

Electrode disks with a diameter of 14 mm are punched from the electrode sheet before drying and bringing into an argon-filled glove box (Mbraun, $\text{H}_2\text{O} < 0.1$ ppm, $\text{O}_2 < 0.1$ ppm). Electrochemical cells are prepared in the glove box using a Li metal counter electrode, 16 μm separator (H1609, Celgard) and 1 M lithium hexafluorophosphate (LiPF_6) in ethylene carbonate (EC): ethyl methyl carbonate (EMC) (30:70 wt.%) with vinylene carbonate (2 wt.%) electrolyte (ELYTE). Coin cells are tested using a battery cycler (LBT21084, Arbin) in a temperature-controlled environment at 20 °C. The mathematical models use the values for cell weight for NMC of 2.19×10^{-7} g, 4.38×10^{-7} g (thickness 80 μm , 160 μm), and LFP of 1.84×10^{-8} g (thickness 90 μm). Further details of the NMC and LFP half cells are shown in Tables V and VI.

Computed tomography scan acquisition.—Both NMC and LFP microstructures are captured using lab-based nano X-ray tomography. The methodology for NMC microstructure acquisition is described in a previous study,³⁰ while the LFP image is acquired as follows. A small disk-shaped electrode with a diameter of approximately 1 mm is obtained from an electrode sheet. The disk is then affixed to a pin head using a fast-setting epoxy. A micro-milling laser technique is utilised to reduce the diameter of the electrode to about 90 μm , resulting in a pillar-shaped specimen. A lab-based X-ray nano-CT system (Zeiss Xradia Ultra 810 X-ray microscope, Carl Zeiss, CA, USA) is used to scan the LFP electrode pillar. The scan is performed with an isotropic voxel size of 64 nm and a field of view of 64 $\mu\text{m} \times 64 \mu\text{m}$. To collect 1601 sequential projections over a 180° rotation, a quasi-monochromatic X-ray beam with a Cr characteristic emission energy of 5.4 keV is used. Each projection has an exposure time of 140 s.

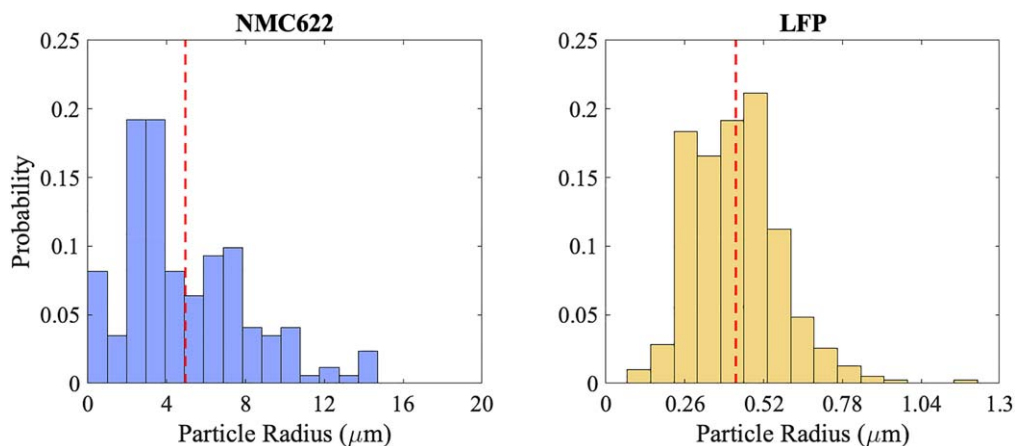


Figure 1. Histograms of the NMC622 and LFP particle radius, obtained from CT scans. The mean radius is given by the red dashed line. The mean NMC particle radius is $4.9 \mu\text{m} \pm 3.1 \mu\text{m}$ and LFP is $0.4 \mu\text{m} \pm 0.1 \mu\text{m}$. There are large particles with radii 14.7 μm and 1.2 μm for NMC and LFP, respectively.

Secondary ion mass spectrometry.—A Thermo Scientific™ Helios™ G4 plasma focused ion beam microscope (PFIB) CXE DualBeam™ system, incorporating a Hidden EQS secondary ion mass spectrometer (SIMS), is used for precise cross-sectioning and spatial mapping of Li across an LFP-based electrode cross-section. The electrode is fabricated using the method described in “LFP Cell Fabrication”. Measurements of the spatially resolved ${}^7\text{Li}^+$ isotope intensity are carried out by application of an acceleration voltage of 30 keV, a probing current of 0.1 nA, resolution of 360 nm and a field of view of 50 $\mu\text{m} \times 105 \mu\text{m}$.

Results and Discussion

Electrode characterisation.—Figure 1 shows the particle radius histograms, measured via X-ray CT imaging, for the particles within the NMC622 and LFP CT image sub-volumes, whose dimensions are outlined in Fig. 2. The NMC and LFP are positive-skewed, with the NMC distribution more positively-skewed than LFP (skewness of 0.96 and 0.79 for NMC and LFP, respectively). The total number of particles is significantly higher within the LFP CT sub-volume (392 particles within a 90 μm thick electrode), compared to NMC CT sub-volume (172 particles within an 80 μm thick electrode), because of the smaller LFP average radius of 0.4 μm compared with 4.9 μm for NMC. There are a small number of particles with radii up to three times the mean radius, especially for NMC where there are eight large particles (larger than 11 μm) including a particle with radius of 14.7 μm . The relatively small LFP particle radii required a nano-CT scanner to resolve, rather than a more commonly available micro-CT scanner. The nano-CT scanner also allowed the acquisition of the CBD in the coarser length-scale NMC electrode. The average electrolyte volume fraction was 0.293 for NMC, obtained from processing CT images as previously described.³³ For LFP, the CBD was not resolved, and a volume fraction of 0.375 (assumed to include the CBD) was obtained.

Modelling results.—We solve the (i) homogenised Doyle-Fuller-Newman model (DFN model), and (ii) microstructurally resolved CT-based model considering the DFN Eqs. (CT model), as described in “Methods”. A total of six cases are considered as shown in Table VII: NMC at 1C and 5C, for electrode thicknesses of 80 μm and 160 μm , and LFP at 2C and 5C for a 90 μm electrode thickness. We compare the model results to experimental data for LFP, while models for NMC have been compared to experiments reported elsewhere.^{24,30} The computational domains for both models are shown in Fig. 2, which also shows the different regions of active particle, carbon binder and pore space.

Figure 3 shows the simulated voltage against capacity for NMC (A) and LFP (B). For NMC in Fig. 3A, the profiles compare well in terms of qualitative shape and predicted capacity, especially at 1C.

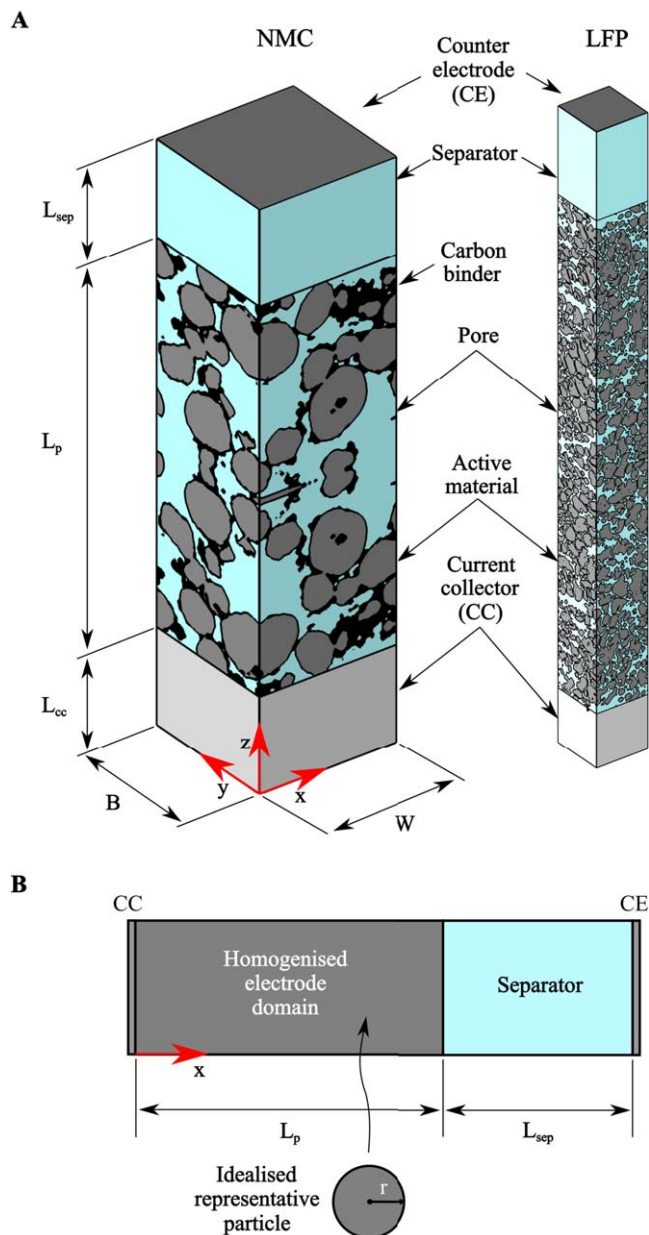


Figure 2. (A) The computational domain for the image-based CT model for NMC ($L_p = 80 \mu\text{m}$ and $160 \mu\text{m}$) and LFP ($L_p = 90 \mu\text{m}$) electrodes. $L_{cc} = 10 \mu\text{m}$ and $L_{sep} = 16 \mu\text{m}$, while $B = W = 30 \mu\text{m}$ for NMC electrodes and $B = W = 10 \mu\text{m}$ for the LFP case. (B) The domain for the pseudo-2D DFN model (Eqs. solved both through the electrode in x and in a representative idealised particle in r), where all relevant dimensions match the microstructural model in (A). The scales are different between sub-figures and is described in more detail in Fig. S1.

Table VII. The six cases considered for modelling for the DFN and CT models.

Case	Chemistry	C rate	Thickness
1	NMC	1C	$80 \mu\text{m}$
2	NMC	5C	$80 \mu\text{m}$
3	NMC	1C	$160 \mu\text{m}$
4	NMC	5C	$160 \mu\text{m}$
5	LFP	2C	$90 \mu\text{m}$
6	LFP	5C	$90 \mu\text{m}$

For LFP in Fig. 3B, the profiles agree with experiment at 5C, while the agreement of the 2C profile is reduced because the experimental training data for model parameterisation was taken at 5C. The

voltage response shows a sharp drop in capacity at 5C for the $160 \mu\text{m}$ thick NMC electrode, and at 5C for the $90 \mu\text{m}$ thick LFP electrode. This drop in capacity is indicative of under-utilization of the active particles, where the normalised particle concentration has not reached unity throughout the electrode. This arises because of Li ion concentration depletion in the electrolyte, where the local Li^+ concentration tends to zero.

Supplementary Fig. S2 shows the originally validated CT model against the NMC622 experimental data (for an electrode thickness of $40 \mu\text{m}$ ³⁰) for voltage profiles with capacity including discharge rates of 0.1C, 1C and 5C and we have included the DFN model used in this work. The models compare well to each other and to the experimental data. Considering the fundamental differences between the two models, in terms of homogenised (DFN) or microscopic (CT), the voltages in Figs. 3 and S2 are encouragingly similar. The results of the two models utilising similar parameters underline the importance of correctly specifying critical parameters and functions

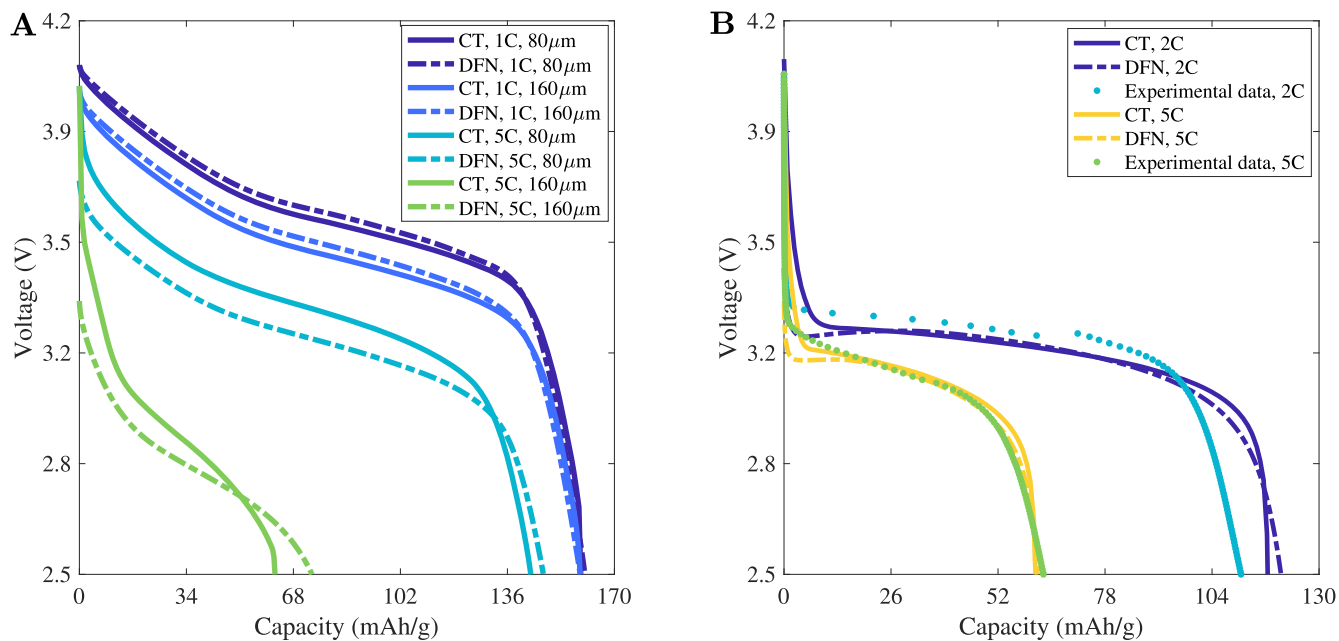


Figure 3. Voltage profiles with capacity for NMC (A) and LFP at 90 μm (B). NMC622 and LFP are characterised by specific capacities at 0.05C of 175 mAh/g and 150 mAh/g, respectively.

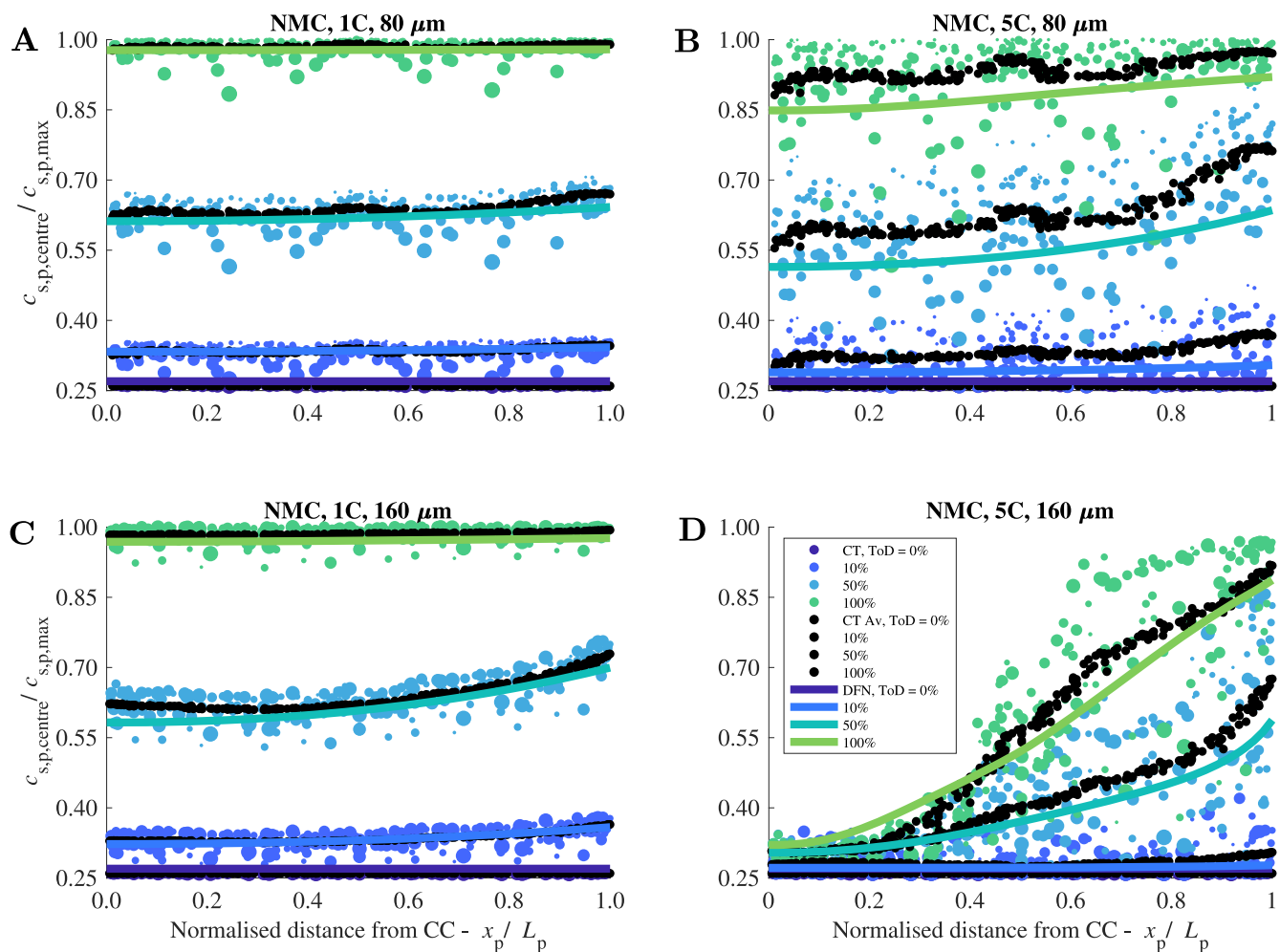


Figure 4. Simulated normalized Li⁺ concentration at the centre of NMC particles - 1C, 80 μm (A), 5C, 80 μm (B), 1C, 160 μm (C), and 5C, 160 μm (D), at range of ToD (time of discharge). The normalized Li⁺ concentration at the centre of the particle ($c_{s,p,centre}/c_{s,p,max}$) is shown as a function of distance from the current collector. 0% ToD is the start of discharge and 100% is the end. DFN model results are represented by solid lines and CT model results are represented by dot markers. The CT model results also indicates the particle radius shown with the marker size, along with the moving average of the concentration shown in black. The moving average is obtained from 31 (A,B) or 51 (C,D) particles. The current collector (CC) is on the left and separator on the right of each subfigure.

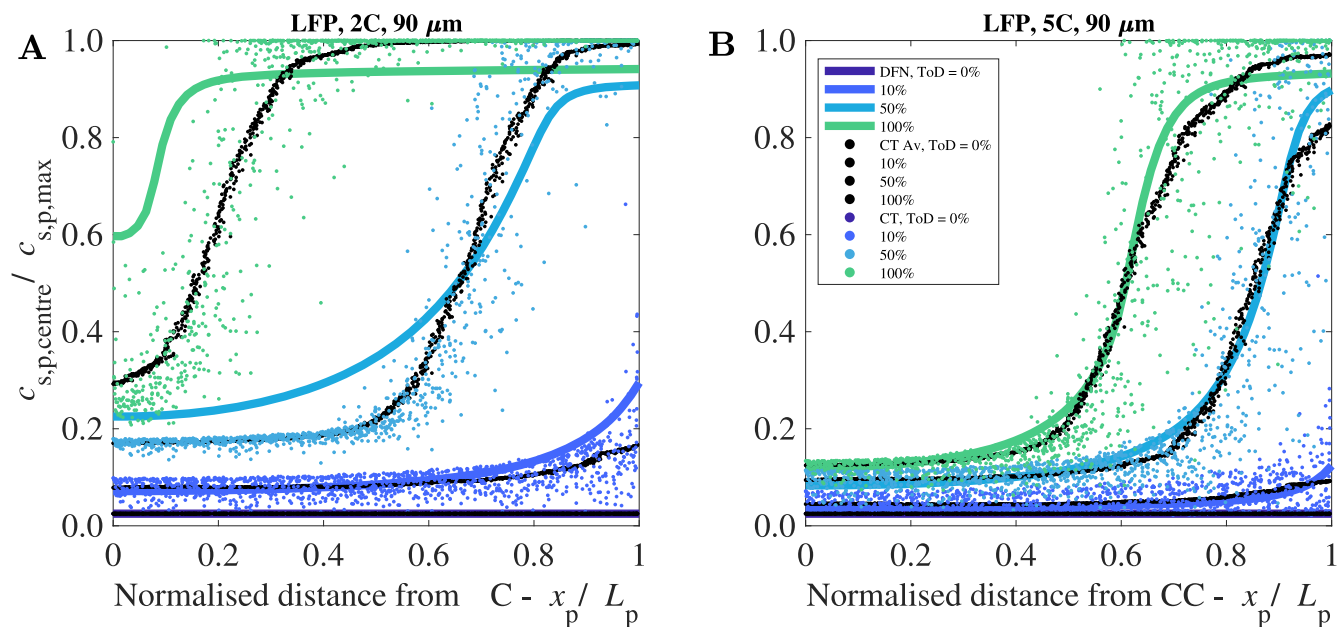


Figure 5. Simulated normalised Li^+ concentration at the centre of LFP particles - 2C (A) and 5C (B), at range of ToD, across a $90 \mu\text{m}$ electrode. The normalised Li^+ concentration at the centre of the particle ($c_{s,p,\text{centre}}/c_{s,p,\text{max}}$) is shown as a function of distance from the CC. 0% ToD is the start of discharge and 100% is the end. DFN model results are solid lines and CT model results are points. The CT model concentration moving average is shown in black. The moving average is obtained from 201 particles. The CC is on the left and separator on the right of each subfigure.

in both models, such as the open circuit potential (OCP) function for each chemistry. When testing parameter sensitivities, the geometric factors such as tortuosity and volume fraction⁵⁴ are important especially at high C rates and can limit capacity, but since the two models are based on similar parameters, these did not result in significant differences. Although the geometric domain of the two models are different, this did not relate to a significant difference in the modelling outcomes, which implies other factors such as the OCP curve,²⁴ are more dominant in determining voltage results.

Figures 4 and 5 show the simulated Li active particle concentrations at the centre of the particle for NMC and LFP, respectively, as a function of distance through the electrode thickness at different time of discharges (ToD). The DFN model is shown as solid lines, while the CT results are shown as dots from individual particles, where the size of the dot is related to the particle radius. The moving averages of the particle concentrations for the CT model results are shown as black points. In all cases, the CT results show that, as expected, the smaller particles lithiate faster than the larger particles. For NMC in Fig. 4, there is good agreement between the DFN and CT models, particularly at 1C in (A) and (C). As the DFN model is solved using an average approach, including the mean particle radius of the CT image data, this supports the good agreement to the CT moving average as expected. At 5C in (B) and (D), the agreement is close to the moving average, but there is a larger distribution of Li^+ concentrations produced with the CT model. At the largest electrode thickness and C rate in (D), the Li^+ concentration profile becomes noticeably sloped, with regions close to the current collector at much lower concentration than close to the separator. The particles are not fully discharged through the thickness of the electrode and through the particle radius, which represents significant under-utilization of active particles related to electrolyte depletion. At 5C and $160 \mu\text{m}$ for NMC, the DFN model fit compared to the CT model is somewhat reduced in terms of the achieved capacity in Fig. 3A, along with Li^+ concentration in the particle in Fig. 4D near the current collector, both at the end of discharge. Small changes to porosity and reaction rate constant (changed to $\varepsilon_{\text{CBD},p} = 0.18$, $\varepsilon_{e,p} = 0.293$ and $k_p = 9 \times 10^{-12} \text{ m}^2 \cdot \text{s}^{-1} \cdot \text{mol}^{-0.5}$) alleviate these differences, but reduce the fit at lower C rates so these changes were not retained.

Table VIII. Number of fitted parameters for the DFN and CT models.

	DFN	Total	CT	Total
NMC622	$b_p, k_p, R_c, \varepsilon_{\text{CBD},p}$	4	k_p, σ_{CBD}	2
LFP	$\varepsilon_{e,p}$	1	$b_p, D_{s,p}, k_p, \varepsilon_{\text{CBD},p}$	4

For LFP in Fig. 5, the slope of the profiles are markedly different with an “S” shape or travelling front across the electrode thickness as the discharge proceeds, approximately segregating discharged and charged regions of the electrode. This distinctive shape arises from the voltage plateau in the OCP profile.²⁴ As seen earlier in the voltage profiles, for 5C in Fig. 5B, there is better agreement than at 2C (A) because the model parameters were fitted at 5C. Supplementary Fig. S3 shows the simulated state of charge (SOC) for LFP compared with the SOC estimated experimentally (calculated based on measured capacity). The modelled SOC profiles agree with one another, and with the experimental data. At 2C, the SOC changes by approximately 80% across the cycle, while at 5C, the SOC changes by only 40% because of increased electrolyte depletion and active material under-utilization.

Figure 6 shows the CT model results for the normalised Li^+ concentration of the active particles for NMC (A) and LFP (B) (whereas Figs. 4 and 5 showed only the centre). The thinner $80 \mu\text{m}$ NMC electrode (A) is the only case that is fully discharged at 100% ToD, represented by a single color throughout and indicating full lithiation. For a $90 \mu\text{m}$ thick LFP electrode (B), the active particles are close to being completely lithiated at the end of discharge, but a through thickness Li^+ gradient has developed as previously described. For the same electrode at 5C, only particles approximately half way across the electrode are significantly lithiated by the end of discharge at 100% ToD. A similar profile arises for a $160 \mu\text{m}$ thick NMC electrode (A). Supplementary Fig. S4 shows the Li^+ concentrations through the solid particle radius for LFP. Encouragingly, when comparing Fig. 6B to Supplementary Fig. S4, the DFN and CT

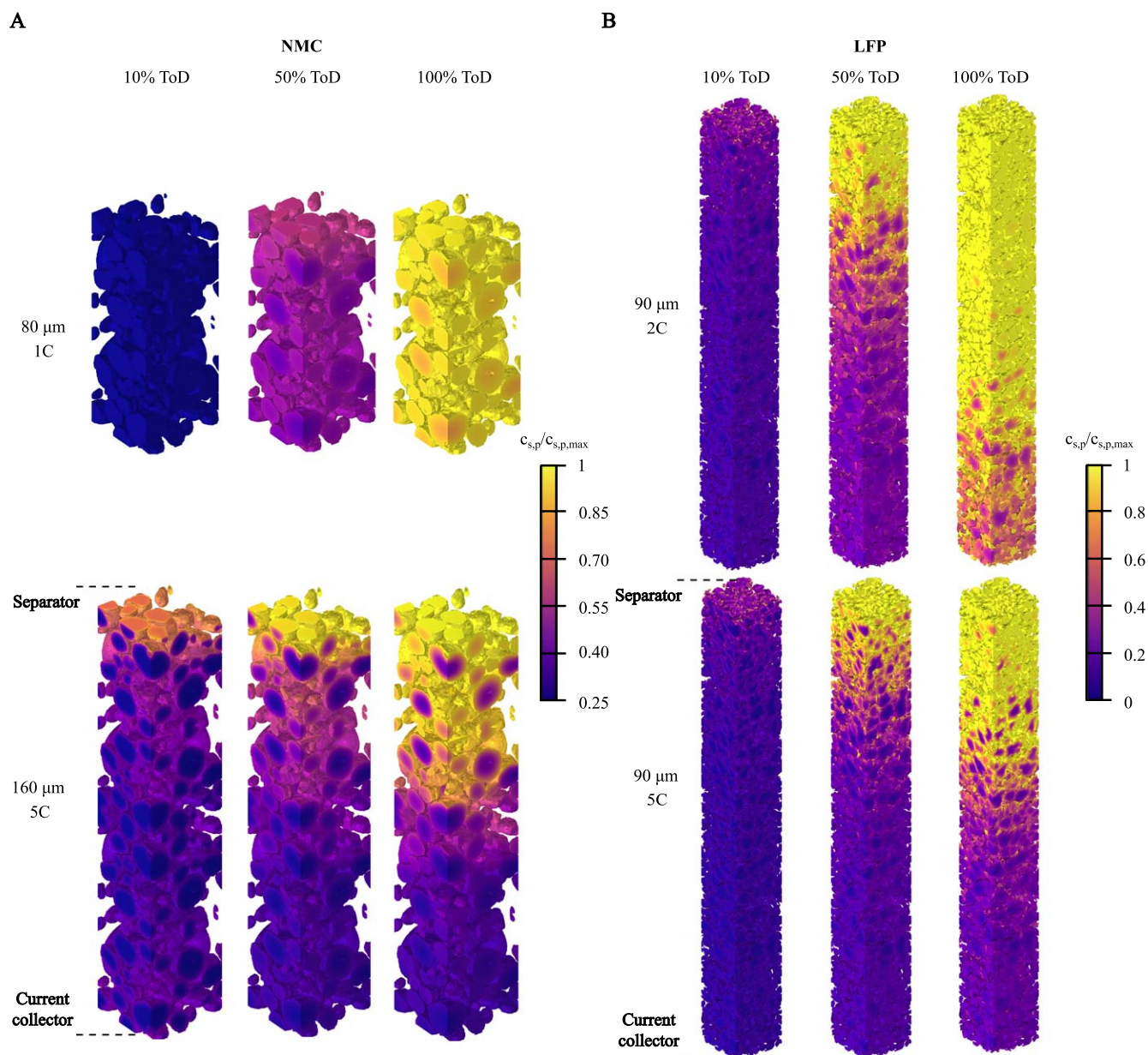


Figure 6. 3D CT model results for normalised Li^+ concentration in the active particles ($c_{s,p}/c_{s,p,\max}$) for NMC (A) and LFP (B). The Figs. are not plotted at the same scale.

models produced similar Li^+ concentrations through the solid particle radius. Both models show that the concentration is either relatively constant near the separator and current collector, or has a gradient near the centre of the electrode, further confirming the similarities in the modelling results.

Figure 7 shows the simulated concentration of Li^+ in the electrolyte through the electrode thickness for NMC and LFP as a function of discharge time. The DFN and CT results compare well over both space and time. All subfigures exhibit complete Li ion concentration depletion, except for the case of 80 μm thick NMC electrode at 1C (A). The Li^+ concentration in the electrolyte for LFP (C,D) changes with time more significantly than NMC, whereas NMC (A,B) quickly reaches a steady-state, especially for 1C (A), where the steady-state has been reached after 10% ToD. The CT model for LFP has a smaller range in concentrations at a particular point in the electrode and a specific ToD. For the CT model for NMC (A, B), there are a range of concentrations at a particular point in the electrode and a specific ToD, because of the wide range of particle radii and pore sizes. The shape of the concentration of active

material and electrolyte profiles (Figs. 7 and 5) for low and high C rates for LFP are similar to those found elsewhere,⁵⁵ comparing to their experimentally relevant solid conductivity values.

Figure 8 shows a comparison of the simulated through thickness Li^+ concentration for the CT model (A), SIMS Li^+ mapping (B), and DFN model (C), for an LFP, 90 μm thick electrode at the end of a 5C discharge. The model shows the normalised Li^+ concentration of active particles ($c_{s,p}/c_{s,p,\max}$), and the SIMS plot is the normalised intensity of the $^7\text{Li}^+$ signal from the particles (after the electrolyte was dried in a protective atmosphere). Consistent with the “S” shape, or travelling front, of the Li^+ concentration profile for LFP described earlier (Fig. 5), there are two reasonably well delineated regions of high and low concentration, with a gradual region approximately at the centre of the electrode thickness. The regions of relatively high Li^+ concentration near the separator are similar across the subfigures. Supplementary Fig. S5 compares modelling and SIMS with the relatively distinct high and low relative Li^+ concentration regions corresponding reasonably well. The through thickness position of the relatively sharp expected transition between low

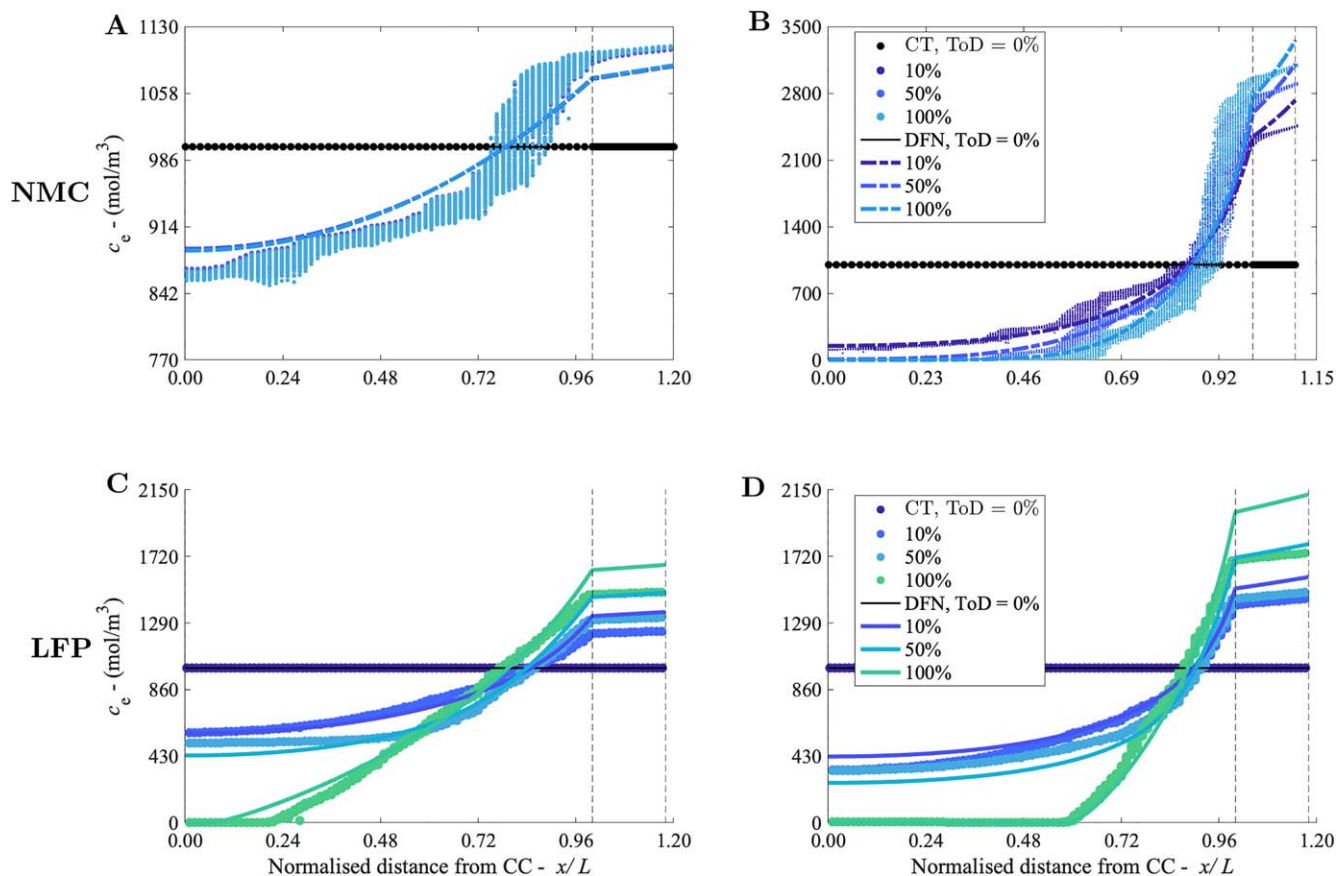


Figure 7. Simulated Li^+ electrolyte concentration (c_e) of NMC electrodes at 1C, 80 μm (A), 5C, 160 μm (B), and LFP at 2C, 90 μm (C), 5C, 90 μm (D), at range of ToD (time of discharge). The CT model is shown as points and DFN as solid lines. The CC is on the left and separator on the right.

and high regions was slightly closer to the separator in the experiment. Given that the SIMS results were not used for the model fitting (voltage measurements were used instead), these independent results are positive. Qualitatively, the comparison between experiment and both models is encouraging and represents a comparatively rare study of simulation and experiments of spatially resolved, Li^+ ion dynamics. Using LFP as the active material together with a relatively high C rate and thick electrode is useful for this type of qualitative comparison because the shape of the open circuit potential with a long plateau of constant voltage leads to a distinct separation between charged and uncharged regions across the electrode thickness at intermediate states of charge.

Table VIII shows the total number of parameters required to be fitted to experimental data for each model. The number of fitted parameters are generally similar, with the CT model for NMC and the DFN model for LFP having the lowest number of parameters (2 and 1, respectively). For the least number of fitted parameters of the DFN model for LFP in Table VIII, all except one parameter was able to be obtained from the CT imaging and model directly. However, due to the large range of NMC particle diameters and that the CBD and electrolyte volume fractions were defined explicitly, the DFN model was not able to directly use as many of the CT parameters. The fitting of the models to LFP experimental data started by (i) using the DFN model to find a baseline set of parameters, (ii) further refining the parameters using the CT model and calculating averaged parameters from the CT results, and then (iii) the parameters refined by the CT model where possible to use in the DFN model (for example the radius of the particle, R_p , carbon binder domain volume fraction, $\varepsilon_{\text{CBD},p}$, tortuosity, b_p , and reaction rate constant, k_p). This shows the benefits of coupling a CT-image based model with a DFN model, and vice versa; using a homogenised DFN model to first find parameters as a basis for the CT model. To reduce the number of

fitted parameters further, additional experiments could be undertaken, for example, to obtain directly values for internal resistance, R_c , and NMC electronic conductivity in the CBD, σ_{CBD} , LFP particle diffusivity, $D_{s,p}$, and tortuosities.^{54,56}

Conclusions

The dynamic responses of the LFP and NMC-based LIB electrodes have been simulated by Doyle-Fuller-Newman and CT-based models. For the six electrode cases investigated, the relatively simple DFN model incorporates sufficient homogenised microstructural detail to agree with the detailed microstructural descriptions available in the CT model. Both models can explain experimental data suggesting that they have sufficiently captured the governing mechanisms of lithium ion electrode dynamics. The CT and DFN models agree well for NMC and LFP based electrodes in terms of voltage response, particle and electrolyte Li concentration, and state of charge. The models also agree qualitatively with the SIMS mapping of $^7\text{Li}^+$ across the thickness of an LFP-based electrode. The DFN model is useful for rapid optimisation and design of battery electrodes and reveals internal electrode dynamics such as critical spatial distributions of Li ion concentration in the electrolyte and particles. The image-based model is capable of capturing and predicting heterogeneities in electrode performance that are important in electrode degradation and operation of batteries under more demanding conditions, such as high current densities.^{33,57} The DFN model requires 20 s (NMC) and 50 s (LFP), and 2.5 GB on a desktop computer, while the CT model requires 8 h (NMC) and 15 h (LFP), and 100 GB random access memory to execute on a high-performance computer. As computing capabilities and CT-scanners continue to increase in power, resolution and availability, while reducing in cost, the CT model approach can be expected to utilised

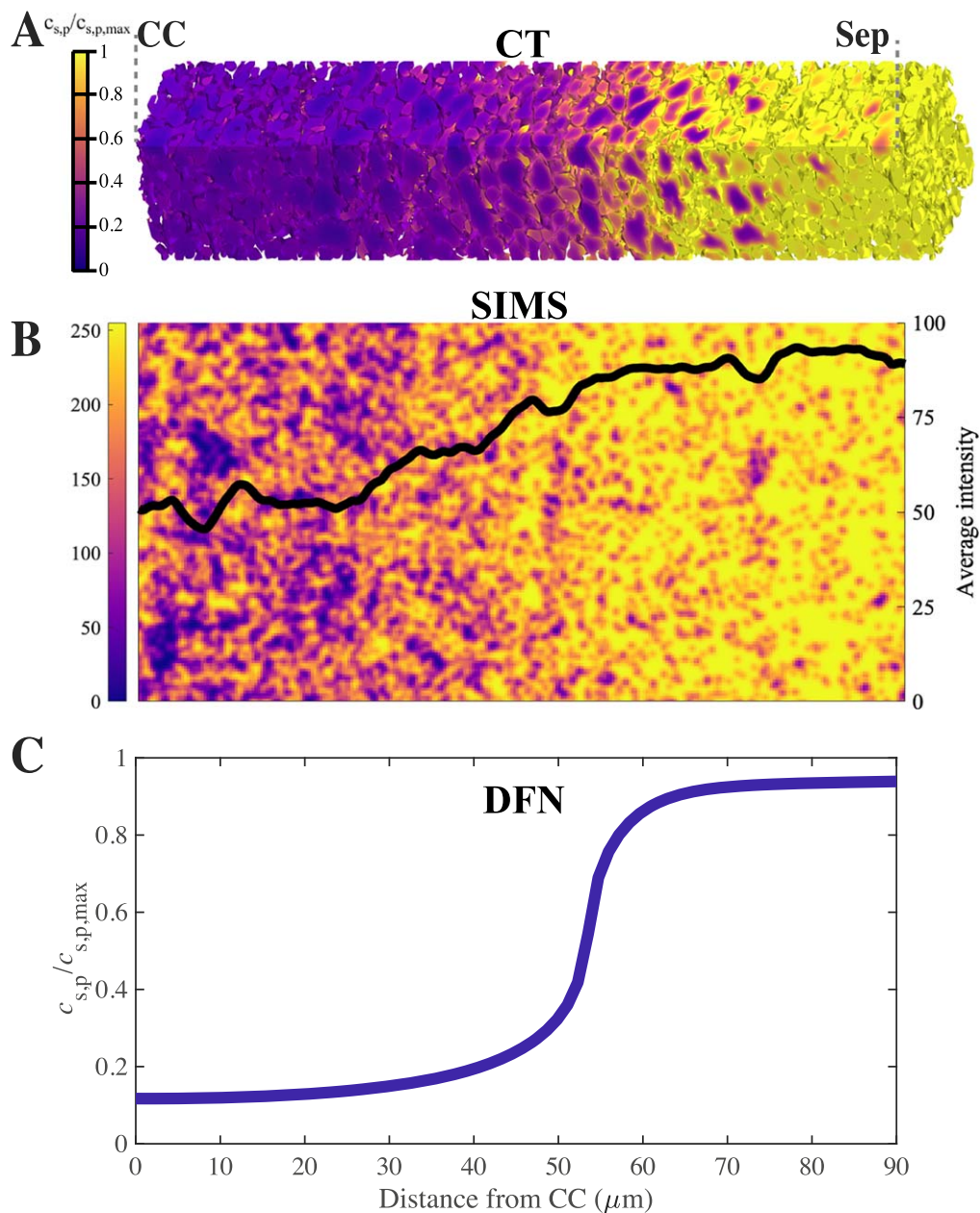


Figure 8. Lithium ion concentration of active particles for a 90 μm thick LFP electrode at 5C discharge, at the end of discharge (100% ToD). (A) and (C) are the simulated normalised Li^+ concentration of solid particles, $c_{s,p}/c_{s,p,\text{max}}$ for the CT model and DFN model ($c_{s,p}$ for the DFN model is integrated over the particle radius). (B) SIMS mapping of $^7\text{Li}^+$ presented as an 8-bit color map with pixel value ranging from 0 to 255, along with the plot of the normalised moving average of the Li^+ ion intensity ($n = 11$). The averaged intensity is calculated by dividing by the maximum of the original data (255), then calculating the average of each column, then the moving average. (C) is the Li^+ concentration over the particle radius for the DFN model. The subfigures have been aligned at the ends of the electrode, with error of $\pm 1 \mu\text{m}$ and show the electrode thickness with the electrode side near the current collector (CC) on the left and near the separator on the right. The results in (A) are replotted from Fig. 6 (B). Supplementary Fig. S5 shows these results in a single figure.

more commonly. We have demonstrated how the DFN and CT models can interact beneficially when parametrising the models. Future work might include a 3D homogenised DFN model that could be utilised to tailor local microstructure variations, allowing simulation of non-spherical particles, as well as degradation effects including cracking and swelling.^{3,21}

Acknowledgments

The authors acknowledge funding provided by the Faraday Institution for project NEXTRUDE (Grant number: FIRG015 and FIRG066). RD acknowledges funding by a UKIC Research Fellowship from the Royal Academy of Engineering. PRS acknowledges funding

from The Royal Academy of Engineering (CiET1718/59). YS acknowledges the use of characterization facilities and valuable discussion within the David Cockayne Centre for Electron Microscopy, Department of Materials, University of Oxford, alongside financial support provided by the Henry Royce Institute (Grant ref EP/R010145/1) and a David Cockayne Fellowship at Linacre College, University of Oxford.

The data that support the findings of this study are available from the corresponding authors upon reasonable request. The DFN simulation and post-processing codes that have been used to produce the results of this study are available as open-source code by author E. C. Tredenick (https://github.com/EloiseTredenick/DFN-P2D-Matlab-NMC622-LFP_CTvsDFN) and the CT model upon reasonable request.


Author contributions

ECT is responsible for DFN model adaptation, project concept, DFN computational code creation, results, analysis, article editing and revision, project management and article writing. AMB is responsible for article writing, project concept, CT scan model adaptation, CT computational code creation, results, analysis, article editing and revision. SW is responsible for experimental data collection for LFP, article writing and reviewing. JL is responsible for experimental data collection for CT scans, and article writing and reviewing. YS is responsible for PFIB and SIMS data collection and analysis, article editing and revision. RD is responsible for model adaptation, article writing, analysis, article editing and revision. SRD, PSG and PRS are responsible for supervision, analysis, article editing and revision.

Competing Interests

The authors declare no competing interests.

ORCID

E. C. Tredenick  <https://orcid.org/0000-0001-9105-2858>
 A. M. Boyce  <https://orcid.org/0000-0002-8164-1808>
 S. Wheeler  <https://orcid.org/0000-0002-4503-4621>
 Y. Sun  <https://orcid.org/0000-0001-8661-8642>
 R. Drummond  <https://orcid.org/0000-0002-2586-1718>
 S. R. Duncan  <https://orcid.org/0000-0002-9525-7305>
 P. S. Grant  <https://orcid.org/0000-0002-7942-7837>
 P. R. Shearing  <https://orcid.org/0000-0002-1387-9531>

References

- McKinsey and Company, "Battery 2030: Resilient, sustainable, and circular." (2023).
- P. S. Grant et al., *J. Phys.: Energy*, **4**, 042006 (2022).
- F. B. Planella et al., *Progress in Energy*, **4**, 042003 (2022).
- J. Scharf et al., *Nat. Nanotechnol.*, **17**, 446 (2022).
- J. M. Reniers and D. A. Howey, *Applied Energy*, **336**, 120774 (2023).
- M. Z. Bazant, *Acc. Chem. Res.*, **46**, 1144 (2013).
- L. M. Morgan et al., *Progress in Energy*, **4**, 012002 (2021).
- S. Nejad, D. Gladwin, and D. Stone, *Journal of Power Sources*, **316**, 183 (2016).
- X. Hu, S. Li, and H. Peng, *Journal of Power Sources*, **198**, 359 (2012).
- G. L. Plett, (University of Colorado) (2015).
- T. Tranter et al., *Journal of Open Source Software*, **7**, 4051 (2022).
- S. Atlung, K. West, and T. Jacobsen, *J. Electrochem. Soc.*, **126**, 1311 (1979).
- S. J. Moura, F. B. Argomedo, R. Klein, A. Mirtabatabaie, and M. Krstic, *IEEE Transactions on Control Systems Technology*, **25**, 453 (2016).
- S. G. Marquis, V. Sulzer, R. Timms, C. P. Please, and S. J. Chapman, *J. Electrochem. Soc.*, **166**, A3693 (2019).
- G. Richardson, I. Korotkin, R. Ranom, M. Castle, and J. Foster, *Electrochimica Acta*, **339**, 135862 (2020).
- M. Guo, G. Sikha, and R. E. White, *J. Electrochem. Soc.*, **158**, A122 (2010).
- G. Ning and B. N. Popov, *J. Electrochem. Soc.*, **151**, A1584 (2004).
- J. M. Reniers, G. Mulder, and D. A. Howey, *J. Electrochem. Soc.*, **166**, A3189 (2019).
- L. D. Couto, J. Schorsch, N. Job, A. Léonard, and M. Kinnaert, *Journal of Energy Storage*, **21**, 259 (2019).
- M. Doyle, T. F. Fuller, and J. Newman, *J. Electrochem. Soc.*, **140**, 1526 (1993).
- H. Arunachalam and S. Onori, *IEEE Conference on Decision and Control (CDC) (IEEE) Vol 2018*, p 5702 (2018), <https://ieeexplore.ieee.org/stamp/stamp.jsp?arnumber=8619793>.
- V. Sulzer, S. G. Marquis, R. Timms, M. Robinson, and S. J. Chapman, *Journal of Open Research Software*, **9**, 14 (2021).
- J. Newman, *DualFoil FORTRAN Programs for the Simulation of Electrochemical Systems* (1998), Available at <http://cchem.berkeley.edu/jsngrp/fortran.html>.
- E. Tredenick, S. Wheeler, R. Drummond, Y. Sun, S. Duncan, and P. Grant, *J. Electrochem. Soc.*, **171** (2024).
- T. L. Kirk, J. Evans, C. P. Please, and S. J. Chapman, *SIAM Journal on Applied Mathematics*, **82**, 625 (2022).
- A. Schmidt, E. Ramani, T. Carraro, J. Joos, A. Weber, M. Kamlah, and E. Ivers-, *Tiffée Energy Technology*, **9**, 2000881 (2021).
- I. Squires, J. M. Foster, A. Galvis, and S. J. Cooper, *J. Electrochem. Soc.*, **171**, 050536 (2024).
- P. Ombrini, M. Z. Bazant, M. Wagemaker, and A. Vasileiadis, *Computational Materials*, **9**, 148 (2023).
- S. Dargaville and T. W. Farrell, *J. Electrochem. Soc.*, **157**, A830 (2010).
- A. M. Boyce, X. Lu, D. J. Brett, and P. R. Shearing, *Journal of Power Sources*, **542**, 231779 (2022).
- X. Lu et al., *Nat. Commun.*, **11**, 2079 (2020).
- X. Lu et al., *Nat. Commun.*, **14**, 5127 (2023).
- A. M. Boyce, E. Martínez-Pañeda, A. Wade, Y. S. Zhang, J. J. Bailey, T. M. Heenan, D. J. Brett, and P. R. Shearing, *Journal of Power Sources*, **526**, 231119 (2022).
- A. G. Kashkooli, S. Farhad, D. U. Lee, K. Feng, S. Litster, S. K. Babu, L. Zhu, and Z. Chen, *Journal of Power Sources*, **307**, 496 (2016), 3.
- J. S. Lopata, T. R. Garrick, F. Wang, H. Zhang, Y. Zeng, and S. Shimpalee, *J. Electrochem. Soc.*, **170**, 020530 (2023).
- T. Danner, M. Singh, S. Hein, J. Kaiser, H. Hahn, and A. Latz, *Journal of Power Sources*, **334**, 191 (2016).
- K. Higa, S.-L. Wu, D. Y. Parkinson, Y. Fu, S. Ferreira, V. Battaglia, and V. Srinivasan, *J. Electrochem. Soc.*, **164**, E3473 (2017).
- A. Latz and J. Zausch, *Beilstein Journal of Nanotechnology*, **6**, 987 (2015).
- T. Sui, B. Song, J. Dluhos, L. Lu, and A. M. Korsunsky, *Nano Energy*, **17**, 254 (2015).
- H. Masuda, N. Ishida, Y. Ogata, D. Ito, and D. Fujita, *Journal of Power Sources*, **400**, 527 (2018).
- Y. Yamagishi, H. Morita, Y. Nomura, and E. Igaki, *ACS Applied Materials & Interfaces*, **13**, 580 (2020).
- H. Xu, J. Zhu, D. P. Finegan, H. Zhao, X. Lu, W. Li, N. Hoffman, A. Bertei, P. Shearing, and M. Z. Bazant, *Adv. Energy Mater.*, **11**, 2003908 (2021).
- R. Franke-Lang, A. Hilger, I. Manke, S. Zavareh, M. F. Bekheet, A. Gurlo, and J. Kowal, *Advanced Theory and Simulations*, **6**, 2300372 (2023).
- The MathWorks Inc., "Matlab version: 9.14.0 (r2023a)." (2023), <https://www.mathworks.com>.
- R. Xu, Y. Yang, F. Yin, P. Liu, P. Cloetens, Y. Liu, F. Lin, and K. Zhao, *Journal of the Mechanics and Physics of Solids*, **129**, 160 (2019).
- A. Jokar, M. Désilets, M. Lacroix, and K. Zaghib, *Journal of Power Sources*, **379**, 84 (2018).
- H. Noh, S. Youn, C. S. Yoon, and Y. Sun, *Journal of Power Sources*, **233**, 121 (2013).
- D. B. Newell et al., "The international system of units (SI)." *NIST Special Publication*, **330**, 1 (2019).
- L. O. Valøen and J. N. Reimers, *J. Electrochem. Soc.*, **152**, A882 (2005).
- M. Farkhondeh, M. Safari, M. Pritzker, M. Fowler, T. Han, J. Wang, and C. Delacourt, *J. Electrochem. Soc.*, **161**, A201 (2013).
- I. Korotkin, S. Sahu, S. E. O'Kane, G. Richardson, and J. M. Foster, *J. Electrochem. Soc.*, **168**, 060544 (2021).
- C. Gao, J. Zhou, G. Liu, and L. Wang, *Appl. Surf. Sci.*, **433**, 35 (2018).
- B. Diouf and R. Pode, *Renewable Energy*, **76**, 375 (2015).
- F. L. E. Usseglio-Viretta et al., *J. Electrochem. Soc.*, **165**, A3403 (2018).
- M. Castle, G. Richardson, and J. M. Foster, *European Journal of App Math*, **33**, 328 (2022).
- F. L. Usseglio-Viretta, D. P. Finegan, A. Colclasure, T. M. Heenan, D. Abraham, P. Shearing, and K. Smith, *J. Electrochem. Soc.*, **167**, 100513 (2020).
- O. O. Taiwo, M. Loveridge, S. D. Beattie, D. P. Finegan, R. Bhagat, D. J. Brett, and P. R. Shearing, *Electrochimica Acta*, **253**, 85 (2017).